Nanoserpents: Graphene Nanoribbon Motion on Two-Dimensional Hexagonal Materials

Wengen Ouyang, Davide Mandelli, Michael Urbakh,* and Oded Hod

School of Chemistry and The Sackler Center for Computational Molecular and Materials Science, Tel Aviv University, Tel Aviv 6997801, Israel

S Supporting Information

ABSTRACT: We demonstrate snake-like motion of graphene nanoribbons atop graphene and hexagonal boron nitride (*h*-BN) substrates using fully atomistic nonequilibrium molecular dynamics simulations. The sliding dynamics of the edge-pulled nanoribbons is found to be determined by the interplay between in-plane ribbon elasticity and interfacial lattice mismatch. This results in an unusual dependence of the friction-force on the ribbon's length, exhibiting an initial linear rise that levels-off above a junction-dependent threshold value dictated by the pre-slip stress distribution within the slider. As part of this letter, we present the LAMMPS implementation of the registry-dependent interlayer potentials for graphene, *h*-BN, and their heterojunctions that were used herein, which provides enhanced performance and accuracy.

KEYWORDS: *Graphene nanoribbons, hexagonal boron nitride (h-BN), registry-dependent interlayer potential, stress distribution, nanoscale friction, LAMMPS*
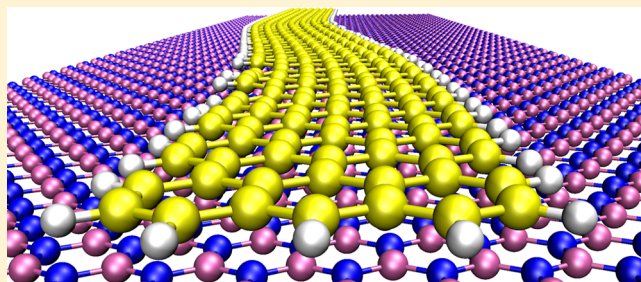
Two-dimensional (2D) layered materials such as graphene, hexagonal boron nitride (*h*-BN), molybdenum disulfide (MoS_2), and tungsten disulfide (WS_2) have attracted great scientific and technological interest due to their unique electronic,[1−3] mechanical,[4−6] and frictional properties.[7−16] In recent years, much attention has been paid to heterogeneous layered materials junctions that may exhibit diverse physical properties as well as enhanced performance over their homogeneous counterparts.[17−19] For instance, recent studies show that graphene/*h*-BN heterostructures may present desired electronic properties[20,21] as well as robust super-lubricity.[22,23]

Further control over the physical properties of 2D layered materials can be gained via tuning their lateral dimensions. To this end, the aspect ratio of graphene nanoribbons (GNRs)[24−27] has been long considered as a handle to control their electronic properties.[28−32] Recently, GNRs have also been shown to exhibit ultralow friction when deposited on gold surfaces.[33−35] This suggests that, when deposited on 2D hexagonal layered materials, where interfacial (in)-commensurability can be controlled, GNR motion should exhibit rich behavior.

In the present letter, we consider the motion of edge-driven graphene nanoribbons atop graphene and *h*-BN substrates. Using fully atomistic molecular dynamics (MD) simulations, we find that the intricate interplay between in-plane ribbon elasticity and interfacial registry results in unique anisotropic snake-like motion. Furthermore, a nonlinear dependence of the friction force on the ribbons' length is predicted, where an

initial increase is followed by the saturation of friction above a junction-dependent characteristic length, which is determined by the interfacial pre-slip stress distribution within the slider.

In order to allow for the elaborate MD simulations undertaken herein, we provide an efficient LAMMPS implementation of the anisotropic interlayer potentials (ILP) for graphene, *h*-BN, and their heterostructures (see Sections 1−3 of the Supporting Information (SI)).[36−38] To enhance the reliability of our calculations we further refine the ILP's parametrization, thus providing a balanced description of the interlayer interactions at both low- and high-pressure regimes.

Our simulated model system consists of an armchair GNR of fixed width (∼0.7 nm) and different lengths in the range of 4− 60 nm sliding atop rigid graphene or *h*-BN monolayer substrates (see Figure 1). The GNR edges are passivated by hydrogen atoms[33] to avoid peripheral C−C bond reconstruction,[39,40] which may influence friction. The GNRs are initially placed atop the graphene or *h*-BN substrates in three different orientations aligning their long axis parallel to the (i) armchair and (ii) zigzag directions of the hexagonal surfaces, as well as (iii) 45° in between them.

The intralayer C−C and C−H interactions within the GNRs were computed via the REBO force field,[41] augmented with a torsion term, which was proposed to improve the description of the mechanical properties of small hydrocarbon molecules.[42]
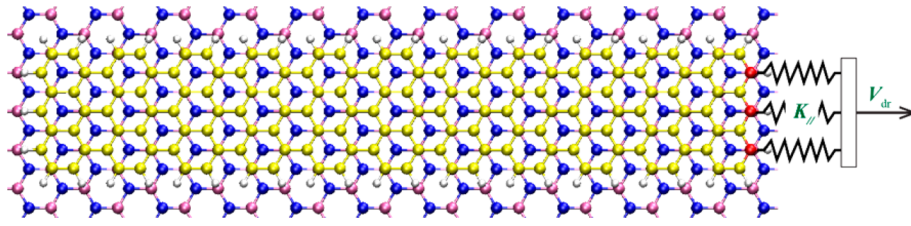
Figure 1. Schematic representation of the simulation setup. A graphene nanoribbon deposited over an h-BN substrate monolayer is driven by a stage moving at constant velocity V_{dr} via springs of stiffness $K_∥$ connected to the three rightmost carbon atoms (red spheres). Mauve, blue, yellow, and gray spheres represent boron, nitrogen, carbon, and hydrogen atoms, respectively.

Test simulations performed neglecting the torsion term yielded quantitatively similar results (see Section 4 of the SI).

The interlayer interactions between the GNRs and the two substrates were described via the registry-dependent ILP,[36−38] which we implemented in the LAMMPS[43] suite of codes. We present a refined parametrization of the ILP and the Kolmogorov Crespi (KC) potential, which provides a balanced treatment of the interlayer interactions in the low and high normal loads regime characterized by interlayer spacing near and below the equilibrium value, respectively. The fitting procedure, the final sets of parameters, the results of several test simulations, and the comparison with the previous parameterizations are discussed in full details in the SI (see Sections 1−3). The results presented herein have been obtained using the ILP parameter set presented in Table S1 of the SI.

All simulations were performed adopting the following protocol. First, we generate the starting configurations of the GNR structures via geometry optimization. This is done using the FIRE algorithm,[44] as implemented in LAMMPS,[43] setting a threshold force value of 10^{-6} eV/Å. Sliding friction simulations are then carried out by attaching the three rightmost carbon atoms of the GNR (red spheres in Figure 1), via springs of constant $K_∥$ in the lateral directions, to a stage of position $r^{stage}(t)$ that is moving along the substrate's armchair axis at constant velocity V_{dr}. The stiffness of the external springs is chosen to be $K_∥ = 3.33$ N/m, resulting in an overall effective spring constant of 10 N/m, close to the typical values used in friction force microscopy (FFM) experiments.[45] Because of numerical limitations, the pulling velocity is chosen to be $V_{dr} = 1$ m/s, which is significantly higher than typical experimental values. Nevertheless, it is sufficiently low to allow for simulating the experimentally observed stick−slip behavior, which is a key feature in the investigated phenomena.

Damped dynamics is applied to avoid junction heating using the following equation of motion:

$$m_i \ddot{r}_i = -\nabla_i (V^{inter} + V^{intra}) - \sum_{\alpha=x,y,z} \eta_\alpha(z_i) m_i \dot{r}_{i,\alpha}$$
$$+ K_∥ (r_i - r^{stage}) \delta_{i,i_{edge}} \qquad (1)$$

where m_i is the mass of atom i, r_i is its position, and V^{inter} and V^{intra} are the interlayer and intralayer interaction potentials, respectively. The second term in eq 1 represents viscous damping applied in all directions $\alpha = x,y,z$ to all GNR atoms, while the last term is the driving spring force, which is applied only to the three rightmost edge atoms in the lateral directions (see Figure 1).

The damping coefficients, $\eta_{x,y,z}$, implicitly account for the dissipation of kinetic energy of the GNR into the microscopic degrees of freedom of the substrate. These are dynamically varied according to the following exponential function:[46−48] $\eta_\alpha(z_i) = \eta_\alpha^0 \exp(1-z_i/d_{eq})$, where z_i is the z coordinate of atom i measured with respect to the substrate surface.

In the case of graphene substrate, the value of d_{eq} is set equal to the density functional theory (DFT) reference equilibrium distance of a graphene bilayer at the energetically optimal AB stacking mode, $d_{eq} = 3.4$ Å (see Section 2 in the SI).[38] In the case of h-BN substrate, d_{eq} is set equal to the DFT reference equilibrium distance of an artificially commensurate graphene/h-BN bilayer at the lattice spacing of 1.43 Å and optimal C-stacking mode, $d_{eq} = 3.3$ Å (see Section 2 in the SI).[37] The results presented in the main text have been obtained using $\eta_x^0 = \eta_y^0 = \eta_z^0 = 1$ ps^{-1}.[49] We checked that the qualitative nature of the simulation results is independent of the choice of η_α^0 within a broad range of values (see Section 5 of the SI).

A fixed time step of 1 fs was used throughout the simulations. To check for convergence of the results with respect to the time-step, we made sensitivity tests by reducing the time step by a factor of 4 leading to practically the same results (see Section 6 of the SI). Unless otherwise stated, all simulations were performed at zero temperature. The static friction force was evaluated from the maximal force experienced by the stage springs obtained prior to the first slip corresponding to the onset of global motion of the GNR. Since the starting configurations were obtained after a careful optimization of the contact geometry, this definition maximizes the obtained static friction forces. Hence, the values presented herein correspond to the minimal force required for the onset of global motion. Alternative definitions for the static friction, such as the average of the force maxima before each slip event during steady-state sliding yield nearly identical results for the systems studied herein.

The time-averaged kinetic friction forces have been calculated as $\langle F_K \rangle = \langle 3K_∥(V_{dr}t - X_{edge}) \rangle$, where $X_{edge} = \sum_{i,edge=1}^{3} x_{i,edge}/3$ is the mean position of the nano-ribbon's edge atoms along the pulling direction and $\langle \cdot \rangle$ denotes a steady-state time average. The statistical errors have been estimated using ten different data sets for every system considered, each taken over a time interval of 1 ns.

Stresses are calculated by dividing the global stress tensor, calculated by LAMMPS and given in units of bar·Å^3,[50] by the volume associated with a carbon atom. The latter is evaluated as $3\sqrt{3}\, a_{CC}^2 h/4$, where $a_{CC} = 1.3978$ Å is the equilibrium C−C distance and $h = 3.35$ Å is the effective thickness associated with the GNR, which we fixed to be equal to the equilibrium interlayer distance of graphite.

We start by investigating the dependence of the static and kinetic friction forces on the ribbon's length (L_{GNR}) for aligned junctions, where the armchair GNR is pulled along the armchair direction of the substrate (see Figure 1). For

nanoscale interfaces, one often finds a typical scaling of the friction force with the contact size ranging from linear in commensurate contacts to sublinear in disordered and incommensurate ones.[22,51−54] As is clearly evident in Figure 2a, b, the aligned motion of GNRs atop graphene or h-BN
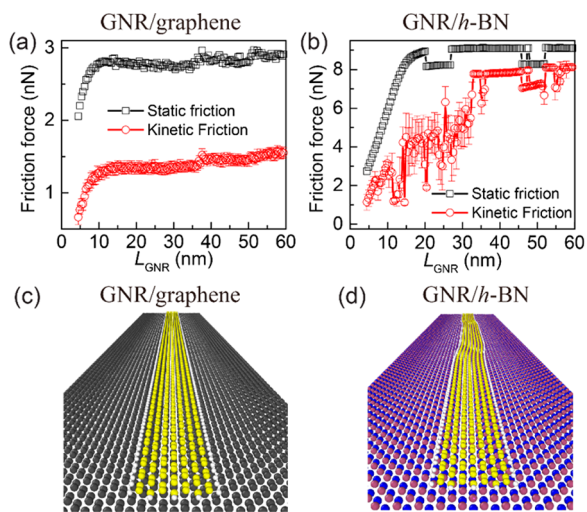

Figure 2. Static (black rectangles) and kinetic (red circles) friction of GNRs sliding over (a) graphene and (b) h-BN as functions of their length. The optimized geometries of a 36.76 nm long armchair GNR deposited along the armchair axis of graphene and h-BN substrates are presented in panels (c) and (d), respectively. Mauve, blue, yellow, and gray spheres represent boron, nitrogen, carbon, and hydrogen atoms, respectively.

surfaces exhibits a qualitatively different behavior. Both aligned junctions display an initial linear increase of the static and kinetic friction forces with the ribbon length (L_{GNR}) that is followed by leveling-off above a characteristic length of $L_{GNR} \approx$ 10 and 20 nm for the homogeneous and heterogeneous interfaces, respectively.

Another counterintuitive behavior that is demonstrated in Figure 2a,b is the fact that at almost any given GNR length, the friction forces of the heterogeneous contact are found to be ∼3-fold larger than those of its homogeneous counterpart. This is in striking contrast with the commonly accepted paradigm that incommensurate interfaces between rigid layered materials should exhibit lower friction than the corresponding homogeneous ones.[8,17,22,55−58] Furthermore, while the homogeneous contact exhibits a smooth variation of the static and kinetic frictional forces with GNR length, the heterojunction shows a much richer behavior, characterized by strong fluctuations of the kinetic friction and sudden jumps of the static friction.

Notably, both aligned homogeneous and heterogeneous junctions also display significantly different relaxed configurations and modes of motion as a function of their length. Upon geometry optimization, all GNRs deposited on a graphene substrate obtain straight configurations (see Figure 2c). On the contrary, when deposited atop of an h-BN substrate, GNRs of length 20.4 nm and beyond exhibit a buckled structure (see Figure 2d). These initial relaxed configurations may be dynamically modified during sliding. When pulled along a graphene substrate, short GNRs keep their straight configuration with negligible structural deformations in the lateral direction perpendicular to the sliding direction (see Supplementary Movie 1). In contrast, beyond a

length of ∼25 nm, the GNRs exhibit shear-induced buckling that results in snake-like motion (see Supplementary Movie 2). A completely different picture arises for GNRs sliding atop an h-BN substrate, where short ribbons exhibit in-plane bending and irregular motion (see Supplementary Movie 3), whereas ribbons of length 35.5 nm and beyond experience shear-induced unbuckling followed by nearly unidirectional motion (see Supplementary Movie 4).

To rationalize these intriguing findings we first analyze the stress distribution along the GNR main axis during the pulling process and its effect on the length-dependence of the frictional forces. Figure 3a,b illustrates the stress distribution
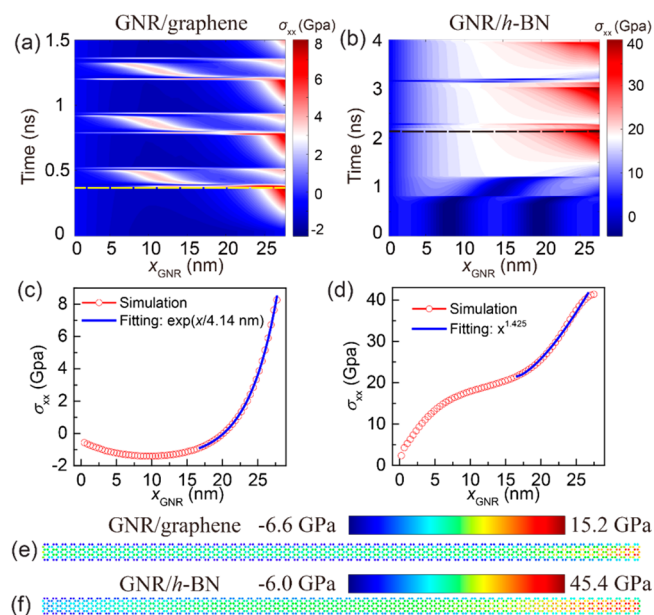

Figure 3. Stress distribution within a 28 nm long GNR sliding atop graphene (left) and h-BN (right) substrates. (a,b) Time evolution 2D color maps of the stress distribution along the GNR, for the homogeneous (a) and heterogeneous (b) junctions. (c,d) Cross section of the above 2D maps at times that correspond to the orange and black horizontal dashed lines of panels (a) and (b), respectively, at the onset of global motion. All stresses reported are calculated by averaging the per-atom stresses along the narrow dimension of the GNR (excluding the passivating hydrogen atoms) and over a single axial unit cell. The position of each axial unit cell along the GNR is calculated as the distance of its center-of-mass from the ribbon's trailing edge. (e,f) Per-atom stress distributions along the GNR that correspond to the onset of sliding of the GNR on graphene and h-BN substrates, respectively (passivating hydrogen atoms are not shown). Note the different scale that the color bars represent in the two panels.

along the GNR as a function of pulling time. Focusing first on the homogeneous junction (Figure 3a) the motion is characterized by stick−slip dynamics. Upon pulling, stress nucleation occurs, growing from the leading edge into the GNR bulk. This is followed by an abrupt stress propagation toward the trailing edge, resulting in a global slip event. We note here that, depending on the local stacking mode, stress may also develop near the center of the GNR. Considering the stress distribution at the onset of sliding, we find that near the pulling edge it can be well fitted with an exponential function (Figure 3c). Hence, we can assess the stress penetration depth to be $L_c \approx 4.14$ nm, which is considerably shorter than the overall ribbon length of 27.5 nm. The former is dictated by the
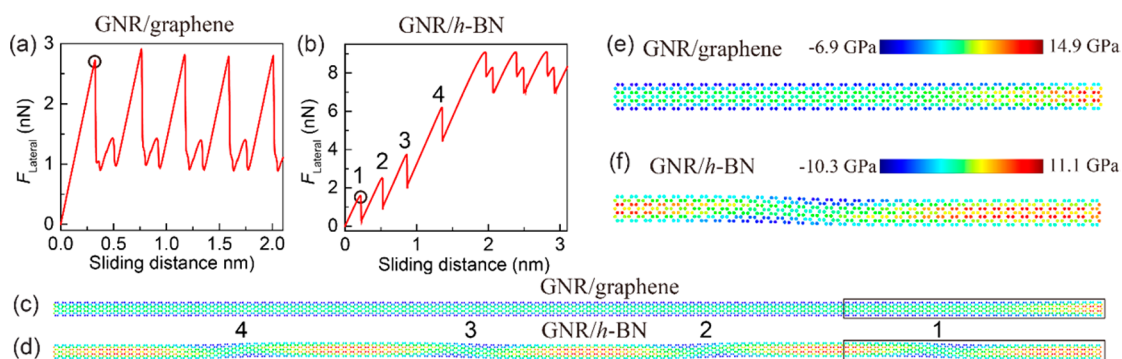
Figure 4. Pulling force as a function of the sliding distance of a GNR deposited over (a) graphene and (b) *h*-BN substrates. (c,d) Corresponding stress distributions of a GNR of length 59.4 nm, computed at the onset of the first (partial) slip event, as indicated by the circles in panels (a) and (b). Panels (e) and (f) provide zoom-in on the rectangular regions highlighted in panels (c) and (d), respectively. Passivating hydrogen atoms are not shown.

ratio between the in-plane GNR stiffness (K_{GNR}) and the ribbon/substrate interaction stiffness ($K_{interface}$) via $L_c = L_{GNR}\sqrt{K_{GNR}/K_{interface}}$ (see Section 8 of the SI for further details).[59]

This observation provides an explanation for the variation of the friction force with ribbon length. For GNRs shorter than the characteristic stress penetration depth a linear increase of both static and kinetic friction forces is obtained, as expected for commensurate junctions. Once the ribbon length exceeds the stress penetration depth, only the atoms in the vicinity of the pulling edge experience stretching and the rest of the bulk atoms remain in their relaxed configuration until the sliding event occurs. Hence, the elastic energy stored during the nucleation stage becomes independent of the ribbon's length, resulting in friction forces leveling off. We note that the residual increase of kinetic friction observed above $L_{GNR} = 40$ nm (see red circles in Figure 2a) is caused by the contribution of the viscous-like dissipation term in eq 1, which is proportional to the number of atoms to which damping is applied.

A qualitatively similar stick−slip behavior is also found for the heterojunction (Figure 3b). However, in this case a much broader nonexponential stress distribution (Figure 3d) is obtained during the nucleation stage. This difference is clearly demonstrated in panels (e) and (f) of Figure 3, where the per-atom stress distribution at the onset of sliding of the heterojunction penetrates much deeper into the GNR bulk than for its homogeneous counterpart. Therefore, the leveling off of the friction forces occurs at a considerably longer GNR length of ∼20 nm (see Figure 2b). We note that the hydrogen passivated edge atoms possess a slightly shorter C−C equilibrium bond distance than their bulk counterparts as indicated by their blue coloring in panels (e) and (f) of Figure 3.

To explain the different relaxed configurations and the irregular behavior of the friction force with ribbon length in the heterojunction (Figure 2b), interfacial commensurability and the formation of moiré superstructures must be taken into account. In the case of extended interfaces, the inherent 1.8% mismatch between graphene and *h*-BN lattice vectors is locally compensated via in-plane deformations. The mating layers form regions of nearly perfect registry and interlayer distance that are separated by elevated ridges to partially alleviate the ensuing strain by exploiting the softer out-of-plane bending modes.[22,60,61] For aligned contacts, the periodicity of these

moiré patterns is $L_{moiré} \approx 14$ nm.[20] In the (quasi)one-dimensional case of the GNR, energy minimization can be achieved not only via in-plane compression and stretching and out-of-plane displacements but also via lateral buckling in the direction perpendicular to the main ribbon axis. For short GNRs (below 20.4 nm for the ribbon width considered herein), the energy cost of such buckling is too high and the ribbon preserves its straight geometry. As the length of the ribbon increases, the competition between the intralayer (elastic) energy and the quest for interlayer registry matching results in the onset of buckling (see Figure 4d,f).

The shear-induced dynamics of these undulations, which share the periodicity of the moiré pattern, are manifested in the length dependence of the static and kinetic friction exhibited by the heterogeneous junction. After reaching the plateau, the static friction shows sharp jumps between two distinct values (∼9.1 and ∼8.3 nN) with increasing ribbon length. The higher (lower) static friction values correspond to GNRs exhibiting even (odd) number of buckles, where the leading edge of the ribbon is positioned in an energetically (un)favorable stacking mode (see corresponding snapshots presented in SI Section 9). During sliding, the interplay between in-plane ribbon elasticity and its interaction with the *h*-BN substrate leads to complex dynamics involving ribbon bending and irregular motion for the shorter GNRs (see Supplementary Movie 3). This dynamics is responsible for the erratic length dependence of the kinetic friction force exhibited by the shorter GNRs (see Figure 2b). A more regular length dependence of the kinetic friction is found for the longer GNRs that exhibit nearly unidirectional steady-state motion (see Supplementary Movie 4).

The origin of the higher friction force exhibited by the heterojunctions with respect to their homogeneous counterparts lies in the difference of the energy barriers encountered during the sliding motion. Previously, we found a similar effect for small two-dimensional graphene flakes sliding atop graphene and *h*-BN surfaces.[22] There, when moving atop graphene, the center of mass of the graphene flake slider performed zigzag type of motion and avoided the global energy barriers resulting in a less corrugated energy path. The sliding energy surface of the heterojunction possessed a more corrugated minimal energy path, thus leading to higher frictional forces. Similar phenomena are obtained for the leading edge of the GNRs studied herein. The GNR head in the homogeneous junction performs noticeable zigzag motion

(see Supplementary Movies 2) to reduce the sliding potential energy barriers along its path and hence reduce the friction. Interestingly, the adaptation of the GNR backbone to its head's rattling translates into the snake-like motion discussed above. In the heterogeneous case, following the initial unbuckling stage, the GNR's head deviates much less from the sliding axis. Hence, its body performs nearly unidirectional motion characterized by a more corrugated sliding energy path and dissipative stick−slip motion (see steady-states in Figure 4a,b and Supplementary Movies 4).

Additional information regarding the shear-induced dynamics of the GNRs can be obtained by further analyzing the friction trace. The aligned homogeneous junctions (see Figure 4c,e) show a very regular double-peaked stick−slip behavior (see Figure 4a). The difference in height of the two peaks reflects the fact that the onset of slip motion results from a pullout of the leading edge atoms from potential energy surface minima of different depth along the sliding path (see Supporting Movie 5). The force traces of the aligned heterogeneous junctions are quite different, exhibiting a sequence of precursor partial slips prior to the onset of global sliding (see Figure 4b). These events reflect the progressive straightening of the ribbons that occurs via successive elimination of the buckled regions (see Figure 4d,f and Supplementary Movie 4), starting from the leading edge and advancing toward the end. Upon complete straightening of the GNR, a global slip event takes place (see Figure 4b). We note that similar force traces, exhibiting partial slip events preceding global sliding, have been observed in macroscale experiments.[62,63] Nevertheless, their origin lies in the evolution of contact area rather than shear-induced unbuckling.

To study the friction dependence on the misfit angle between the ribbon and the surface, we performed similar simulations while pulling the GNRs at two angles of 45° and 90° with respect to the armchair axis of the substrate. As may be expected due to incommensurability considerations, the latter (not shown) exhibit smooth sliding accompanied by ultralow friction regardless of the underlying surface.[8,11,13,64,65] Pulling at the angle of 45° results in a more diverse behavior, as illustrated in Figure 5. Figure 5a,c presents the lateral force traces (red curves) for the homogeneous GNR/graphene junction with ribbon lengths of 4.5 and 27.5 nm, respectively. After a short interval characterized by smooth sliding, a sudden increase of friction occurs, reflecting an abrupt reorientation of the ribbon to achieve an energetically more favorable interfacial registry with the underlying surface (see Figure S13 in section 10 of the SI). As shown by the blue lines in Figure 5a,c, the ribbon rotates from its original 45° alignment to an average angle of ~60° with respect to the armchair direction of the graphene substrate (see also Supplementary Movie 6). Comparing panels (a) and (c), we find that the shorter the GNR, the earlier its reorientation occurs during the dynamics. We note that similar reorientation processes have been observed experimentally and computationally for graphene flakes sliding atop a graphite surface.[66,67]

The shorter heterogeneous GNR/h-BN junction (Figure 5b) exhibits a very similar behavior to that of its homogeneous counterpart with an initial low-friction stage followed by a rotation toward the 60° misaligned configuration that is accompanied by a sharp increase of friction (see Figure 5b,f). On the contrary, the frictional dynamics of the longer heterojunction is characterized by a gradual reorientation process (Figure 5d). This results from the shear-induced
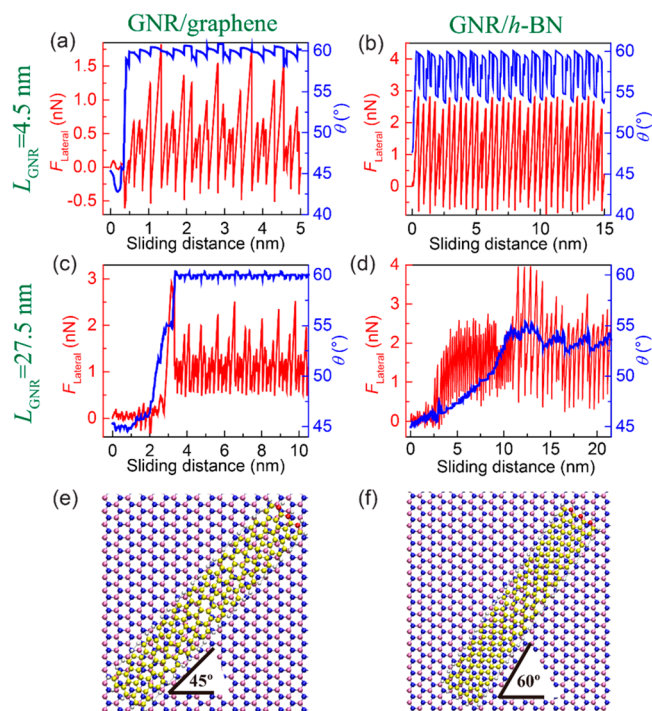

Figure 5. Frictional motion of GNRs pulled along a direction of 45° with respect to the armchair direction of graphene (a,c) and h-BN (b,d) substrates. Both the lateral force (left axis, red) and the average angle (right axis, blue) are presented as a function of sliding distance for L_{GNR} = 4.5 nm (a,b) and 27.5 nm (c,d). The configurations of the shorter GNR on h-BN before (e) and after (f) reorientation are presented for visual demonstration of the effect. Mauve, blue, yellow, and gray spheres represent boron, nitrogen, carbon, and hydrogen atoms, respectively.

dynamics of the ribbon's buckled structure leading to snake-like motion (see Supplementary Movie 7).

Finally, all results presented thus far have been obtained at zero temperature. This allowed for deciphering the main mechanisms underlying the intricate motion of GNRs on graphene and h-BN, while avoiding the complications involved with thermal noise effects. To further evaluate the validity and relevance of the obtained results at room temperature (300 K), we repeated some of the calculations using a Langevin thermostat (see Section 7 of the SI for details on the adopted protocol). Let us first consider the homogeneous contact. Although the measured values of the static and kinetic friction forces decrease by virtue of thermally assisted crossing of the sliding potential energy barriers,[58] we found that the qualitative dependence of the static and kinetic friction forces on the GNR length (see Figure 6a,c), the stick−slip behavior (see Figure 6e), and the serpent-like motion of the longer GNRs (see Supplementary Movie 8) survive also at room temperature. Thermolubricity effects are found to be more prominent in the heterogeneous contact. Even though the stick−slip behavior survives the thermal effects also in this case (see Figure 6f), the static and kinetic friction forces are found to reduce by a larger factor of up to ~4 and ~8, respectively, when compared to the corresponding values at zero temperature (see Figure 6b,d), and friction becomes practically independent of the GNR length. Furthermore, the buckling observed in the equilibrium configuration at zero temperature is washed out by thermal fluctuations. As a consequence, the precursor unbuckling slips observed in the zero temperature
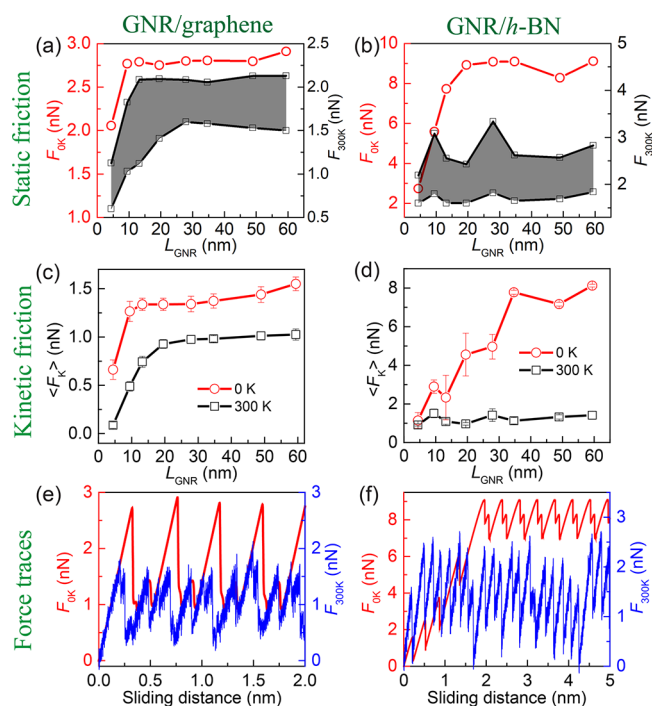
Figure 6. Sensitivity of the friction forces of a GNR/graphene homogeneous junction (a,c,e) and a GNR/h-BN heterogeneous junction (b,d,f) toward the simulated temperature. Shown is the length dependence of the (a,b) static and (c,d) kinetic friction forces of the GNR length calculated at 0 K (red circles) and 300 K (black squares). At zero temperature, the reported values of the static friction correspond to the maximum force before the first slip event. At finite temperature, the stick−slip behavior is erratic, and the values of the maxima of the force before the main slip events become broadly distributed. Here, we provide a crude estimation of the width of this distribution by the shaded area in panels (a) and (b), which indicates the spreading between maximum and minimum of the force measured before the main slip events considering the whole friction trace. The statistical errors for the kinetic friction force have been estimated using ten different trajectories, each averaged over a time interval of 1.5 ns. The force traces of the 59.4 nm long GNR on graphene (e) and h-BN (f) at zero temperature (left axis, red) and room temperature (right axis, blue) are presented as well.

friction trace (red curve in Figure 6f) are absent at room temperature (blue curve in Figure 6f). Notably, at room temperature, the values of both kinetic and static friction of the heterojunction become comparable to those of the homogeneous graphitic interface.

To summarize, quasi-one-dimensional junctions between layered materials introduce an additional degree of freedom over their extended two-dimensional counterparts. Apart from in-plane compression/expansion and out-of-plane corrugation, nanoribbons are allowed to buckle in the direction perpendicular to the sliding motion in order to enhance their registry with the underlying substrate. This leads to new types of driven motion and frictional behavior observed in zero temperature simulations. Specifically, both homogeneous and heterogeneous junctions of a GNR aligned with graphene and h-BN exhibit a length independence of the friction beyond a certain contact size due to the finite penetration of the in-plane stress into the GNR bulk. In the homogeneous case, in order to follow a less corrugated energy path, the ribbon's head performs a zigzag movement, which translates to less dissipative snake-like motion of the longer systems. On the

contrary, the longer heterojunctions exhibit initial shear-induced unbuckling followed by nearly unidirectional dissipative stick−slip motion. The interplay between the stress distribution along the GNR and the lattice mismatch of the contacting surfaces dictates the characteristic length scales at which these phenomena will take place. Misaligned contacts show either ultralow friction or dynamic transition between low and high friction states due to shear-induced reorientations. Finite temperature effects affect only quantitatively the frictional response of homogeneous contacts, where static and kinetic friction reduce by ~50%, but still display the same length dependence observed at zero temperature. However, thermal fluctuations in the heterogeneous junctions lead to a significant reduction of friction by up to a factor of ~8, and both static and kinetic friction become practically independent of GNR length. The simulation of such intricate phenomena became possible by a LAMMPS implementation of our registry-dependent interlayer potential and refinement of its parametrization for bilayer graphene and its heterojunction with h-BN (https://lammps.sandia.gov/doc/pair_ilp_graphene_hbn.html).

■ ASSOCIATED CONTENT

Ⓢ Supporting Information

The Supporting Information is available free of charge on the ACS Publications website at DOI: 10.1021/acs.nanolett.8b02848.

> ILP parameters refinement procedure; benchmark tests for the ILP LAMMPS implementation; sensitivity tests of the results with respect to the ILP parametrization, choice of intralayer potential, values of the damping coefficients and propagation time step; simulation protocol at finite temperature; theoretical estimation of the characteristic stress decay length into the GNR bulk; stacking modes of the GNR's leading edge atop an h-BN substrate and evolution of potential energy during sliding at 45 degrees (PDF)
> Supporting Movies (ZIP)

■ AUTHOR INFORMATION

Corresponding Author

*E-mail: urbakh@post.tau.ac.il. Phone: +9726408324.

ORCID Ⓘ

Wengen Ouyang: 0000-0001-8700-1978

Michael Urbakh: 0000-0002-3959-5414

Oded Hod: 0000-0003-3790-8613

Notes

The authors declare no competing financial interest.

■ REFERENCES

(1) Novoselov, K. S.; Geim, A. K.; Morozov, S. V.; Jiang, D.; Zhang, Y.; Dubonos, S. V.; Grigorieva, I. V.; Firsov, A. A. *Science* **2004**, *306*, 666−669.

(2) Castro Neto, A. H.; Guinea, F.; Peres, N. M. R.; Novoselov, K. S.; Geim, A. K. *Rev. Mod. Phys.* **2009**, *81*, 109−162.

(3) Koren, E.; Leven, I.; Lörtscher, E.; Knoll, A.; Hod, O.; Duerig, U. *Nat. Nanotechnol.* **2016**, *11*, 752.

(4) Meyer, J. C.; Geim, A. K.; Katsnelson, M.; Novoselov, K.; Booth, T.; Roth, S. *Nature* **2007**, *446*, 60−63.

(5) Lee, C.; Wei, X.; Kysar, J. W.; Hone, J. *Science* **2008**, *321*, 385−388.

(6) Falin, A.; Cai, Q.; Santos, E. J. G.; Scullion, D.; Qian, D.; Zhang, R.; Yang, Z.; Huang, S.; Watanabe, K.; Taniguchi, T.; Barnett, M. R.; Chen, Y.; Ruoff, R. S.; Li, L. H. *Nat. Commun.* **2017**, *8*, 15815.

(7) Sheehan, P. E.; Lieber, C. M. *Science* **1996**, *272*, 1158−1161.

(8) Dienwiebel, M.; Verhoeven, G. S.; Pradeep, N.; Frenken, J. W.; Heimberg, J. A.; Zandbergen, H. W. *Phys. Rev. Lett.* **2004**, *92*, 126101.

(9) Lee, C.; Li, Q.; Kalb, W.; Liu, X.-Z.; Berger, H.; Carpick, R. W.; Hone, J. *Science* **2010**, *328*, 76−80.

(10) Cahangirov, S.; Ataca, C.; Topsakal, M.; Sahin, H.; Ciraci, S. *Phys. Rev. Lett.* **2012**, *108*, 126103.

(11) Liu, Z.; Yang, J.; Grey, F.; Liu, J. Z.; Liu, Y.; Wang, Y.; Yang, Y.; Cheng, Y.; Zheng, Q. *Phys. Rev. Lett.* **2012**, *108*, 205503.

(12) Yang, J.; Liu, Z.; Grey, F.; Xu, Z.; Li, X.; Liu, Y.; Urbakh, M.; Cheng, Y.; Zheng, Q. *Phys. Rev. Lett.* **2013**, *110*, 255504.

(13) Koren, E.; Lörtscher, E.; Rawlings, C.; Knoll, A. W.; Duerig, U. *Science* **2015**, *348*, 679−683.

(14) Wang, W.; Dai, S.; Li, X.; Yang, J.; Srolovitz, D. J.; Zheng, Q. *Nat. Commun.* **2015**, *6*, 7853.

(15) Berman, D.; Erdemir, A.; Sumant, A. V. *ACS Nano* **2018**, *12*, 2122−2137.

(16) Martin, J. M.; Erdemir, A. *Phys. Today* **2018**, *71*, 40−46.

(17) Leven, I.; Krepel, D.; Shemesh, O.; Hod, O. *J. Phys. Chem. Lett.* **2013**, *4*, 115−120.

(18) Geim, A.; Grigorieva, I. *Nature* **2013**, *499*, 419−425.

(19) Novoselov, K. S.; Mishchenko, A.; Carvalho, A.; Castro Neto, A. H. *Science* **2016**, *353*, aac9439.

(20) Woods, C. R.; Britnell, L.; Eckmann, A.; Ma, R. S.; Lu, J. C.; Guo, H. M.; Lin, X.; Yu, G. L.; Cao, Y.; Gorbachev, R. V.; Kretinin, A. V.; Park, J.; Ponomarenko, L. A.; Katsnelson, M. I.; Gornostyrev, Y. N.; Watanabe, K.; Taniguchi, T.; Casiraghi, C.; Gao, H. J.; Geim, A. K.; Novoselov, K. S. *Nat. Phys.* **2014**, *10*, 451−456.

(21) Slotman, G. J.; van Wijk, M. M.; Zhao, P. L.; Fasolino, A.; Katsnelson, M. I.; Yuan, S. *Phys. Rev. Lett.* **2015**, *115*, 186801.

(22) Mandelli, D.; Leven, I.; Hod, O.; Urbakh, M. *Sci. Rep.* **2017**, *7*, 10851.

(23) Song, Y.; Mandelli, D.; Hod, O.; Urbakh, M.; Ma, M.; Zheng, Q. *Nat. Mater.* **2018**, DOI: 10.1038/s41563-018-0144-z.

(24) Kosynkin, D. V.; Higginbotham, A. L.; Sinitskii, A.; Lomeda, J. R.; Dimiev, A.; Price, B. K.; Tour, J. M. *Nature* **2009**, *458*, 872.

(25) Cai, J.; Ruffieux, P.; Jaafar, R.; Bieri, M.; Braun, T.; Blankenburg, S.; Muoth, M.; Seitsonen, A. P.; Saleh, M.; Feng, X.; Müllen, K.; Fasel, R. *Nature* **2010**, *466*, 470.

(26) Tao, C.; Jiao, L.; Yazyev, O. V.; Chen, Y.-C.; Feng, J.; Zhang, X.; Capaz, R. B.; Tour, J. M.; Zettl, A.; Louie, S. G.; Dai, H.; Crommie, M. F. *Nat. Phys.* **2011**, *7*, 616.

(27) Ruffieux, P.; Cai, J.; Plumb, N. C.; Patthey, L.; Prezzi, D.; Ferretti, A.; Molinari, E.; Feng, X.; Müllen, K.; Pignedoli, C. A.; Fasel, R. *ACS Nano* **2012**, *6*, 6930−6935.

(28) Son, Y.-W.; Cohen, M. L.; Louie, S. G. *Nature* **2006**, *444*, 347.

(29) Son, Y.-W.; Cohen, M. L.; Louie, S. G. *Phys. Rev. Lett.* **2006**, *97*, 216803.

(30) Ezawa, M. *Phys. Rev. B: Condens. Matter Mater. Phys.* **2006**, *73*, 045432.

(31) Barone, V.; Hod, O.; Scuseria, G. E. *Nano Lett.* **2006**, *6*, 2748−2754.

(32) Hod, O.; Scuseria, G. E. *Nano Lett.* **2009**, *9*, 2619−2622.

(33) Kawai, S.; Benassi, A.; Gnecco, E.; Söde, H.; Pawlak, R.; Feng, X.; Müllen, K.; Passerone, D.; Pignedoli, C. A.; Ruffieux, P. *Science* **2016**, *351*, 957−961.

(34) Gigli, L.; Manini, N.; Benassi, A.; Tosatti, E.; Vanossi, A.; Guerra, R. *2D Mater.* **2017**, *4*, 045003.

(35) Gigli, L.; Manini, N.; Tosatti, E.; Guerra, R.; Vanossi, A. *Nanoscale* **2018**, *10*, 2073−2080.

(36) Leven, I.; Azuri, I.; Kronik, L.; Hod, O. *J. Chem. Phys.* **2014**, *140*, 104106.

(37) Leven, I.; Maaravi, T.; Azuri, I.; Kronik, L.; Hod, O. *J. Chem. Theory Comput.* **2016**, *12*, 2896−905.

(38) Maaravi, T.; Leven, I.; Azuri, I.; Kronik, L.; Hod, O. *J. Phys. Chem. C* **2017**, *121*, 22826−22835.

(39) Faccio, R.; Denis, P. A.; Pardo, H.; Goyenola, C.; Mombru, A. W. *J. Phys.: Condens. Matter* **2009**, *21*, 285304.

(40) Dubois, S. M. M.; Lopez-Bezanilla, A.; Cresti, A.; Triozon, F.; Biel, B.; Charlier, J.-C.; Roche, S. *ACS Nano* **2010**, *4*, 1971−1976.

(41) Brenner, D. W.; Shenderova, O. A.; Harrison, J. A.; Stuart, S. J.; Ni, B.; Sinnott, S. B. *J. Phys.: Condens. Matter* **2002**, *14*, 783−802.

(42) Stuart, S. J.; Tutein, A. B.; Harrison, J. A. *J. Chem. Phys.* **2000**, *112*, 6472−6486.

(43) Plimpton, S. *J. Comput. Phys.* **1995**, *117*, 1−19.

(44) Bitzek, E.; Koskinen, P.; Gähler, F.; Moseler, M.; Gumbsch, P. *Phys. Rev. Lett.* **2006**, *97*, 170201.

(45) Szlufarska, I.; Chandross, M.; Carpick, R. W. *J. Phys. D: Appl. Phys.* **2008**, *41*, 123001.

(46) Zaloj, V.; Urbakh, M.; Klafter, J. *Phys. Rev. Lett.* **1999**, *82*, 4823−4826.

(47) Braun, O. M.; Peyrard, M. *Phys. Rev. E: Stat. Phys., Plasmas, Fluids, Relat. Interdiscip. Top.* **2001**, *63*, 046110.

(48) Ouyang, W.; Ma, M.; Zheng, Q.; Urbakh, M. *Nano Lett.* **2016**, *16*, 1878−1883.

(49) Persson, B. N. *Sliding Friction: Physical Principles and Applications*; Springer Science & Business Media: 2000; Vol. *1*.

(50) Thompson, A. P.; Plimpton, S. J.; Mattson, W. *J. Chem. Phys.* **2009**, *131*, 154107.

(51) Müser, M. H. *Europhys. Lett.* **2004**, *66*, 97−103.

(52) de Wijn, A. S. *Phys. Rev. B: Condens. Matter Mater. Phys.* **2012**, *86*, 085429.

(53) Dietzel, D.; Feldmann, M.; Schwarz, U. D.; Fuchs, H.; Schirmeisen, A. *Phys. Rev. Lett.* **2013**, *111*, 235502.

(54) Koren, E.; Duerig, U. *Phys. Rev. B: Condens. Matter Mater. Phys.* **2016**, *93*, 201404.

(55) Shinjo, K.; Hirano, M. *Surf. Sci.* **1993**, *283*, 473−478.

(56) Verhoeven, G. S.; Dienwiebel, M.; Frenken, J. W. *Phys. Rev. B: Condens. Matter Mater. Phys.* **2004**, *70*, 165418.

(57) Hod, O. *ChemPhysChem* **2013**, *14*, 2376−2391.

(58) Vanossi, A.; Manini, N.; Urbakh, M.; Zapperi, S.; Tosatti, E. *Rev. Mod. Phys.* **2013**, *85*, 529−552.

(59) Capozza, R.; Urbakh, M. *Phys. Rev. B: Condens. Matter Mater. Phys.* **2012**, *86*, 085430.

(60) van Wijk, M. M.; Schuring, A.; Katsnelson, M. I.; Fasolino, A. *Phys. Rev. Lett.* **2014**, *113*, 135504.

(61) Wijk, M. M. v.; Schuring, A.; Katsnelson, M. I.; Fasolino, A. *2D Mater.* **2015**, *2*, 034010.

(62) Rubinstein, S. M.; Cohen, G.; Fineberg, J. *Phys. Rev. Lett.* **2007**, *98*, 226103.

(63) Ben-David, O.; Rubinstein, S. M.; Fineberg, J. *Nature* **2010**, *463*, 76−79.

(64) Li, H.; Wang, J.; Gao, S.; Chen, Q.; Peng, L.; Liu, K.; Wei, X. *Adv. Mater.* **2017**, *29*, 1701474.

(65) Wang, L.; Zhou, X.; Ma, T.; Liu, D.; Gao, L.; Li, X.; Zhang, J.; Hu, Y.; Wang, H.; Dai, Y.; Luo, J. *Nanoscale* **2017**, *9*, 10846−10853.

(66) Filippov, A. E.; Dienwiebel, M.; Frenken, J. W. M.; Klafter, J.; Urbakh, M. *Phys. Rev. Lett.* **2008**, *100*, 046102.

(67) Feng, X.; Kwon, S.; Park, J. Y.; Salmeron, M. *ACS Nano* **2013**, *7*, 1718−1724.